

AaPE: Aliasing-aware Patch Embedding for Self-Supervised Audio Representation Learning

Kohei Yamamoto^{1,2}, Kosuke Okusa²

Abstract—Transformer-based audio SSL (self-supervised learning) models often treat spectrograms as images, applying convolutional patchification with heavy temporal downsampling. This lowers the effective Nyquist frequency and introduces aliasing, while naïve low-pass filtering removes task-relevant high-frequency cues. In this study, we present Aliasing-aware Patch Embedding (AaPE), a drop-in patch stem that mitigates aliasing while preserving high-frequency information. AaPE augments standard patch tokens with features produced by a band-limited complex sinusoidal kernel using a two-sided exponential window that dynamically targets alias-prone bands. Frequency and decay parameters of the kernel are estimated from the input, enabling parallel, adaptive subband analysis whose outputs are fused with the standard patch tokens. AaPE integrates seamlessly into the masked teacher-student self-supervised learning. In addition, we combine a multi-mask strategy with a contrastive objective to enforce consistency across diverse mask patterns, stabilizing training. Pre-training on AudioSet followed by fine-tuning evaluation across diverse downstream benchmarks, which spanned categories, such as environmental sounds and other common audio domains. This approach yields state-of-the-art performance on a subset of tasks and competitive results across the remainder. Complementary linear probing evaluation mirrors this pattern, yielding clear gains on several benchmarks and strong performance elsewhere. The collective analysis of these results indicates that AaPE serves to mitigate the effects of aliasing without discarding of informative high-frequency content.

Index Terms—Self-supervised learning, masked audio modeling, transformers, aliasing, structured state-space models.

I. INTRODUCTION

RECENT advances in natural language processing (NLP) and computer vision demonstrate the effectiveness of self-supervised learning (SSL), thereby training neural networks from unlabeled data via auxiliary objectives. SSL has achieved strong results in NLP [1] and vision [2], and currently is advancing audio research [3]–[7], improving downstream tasks, such as acoustic recognition, event detection, and captioning. In the domain of audio, transformer models operating on spectrograms have demonstrated efficacy in learning high-level semantic representations [8]. Treating spectrograms as two-dimensional images enables the adaptation of Vision Transformer (ViT) [9] and Masked Image Modeling (MIM) [10] methods to audio, broadening the scope of acoustic representation learning [3], [4].

Despite the efficacy of Transformer features, a key limitation lies in how spectrograms are patchified for input embeddings. Typical pipelines apply a convolutional stem layer that patches the spectrogram while aggressively downsampling the time axis (often by a factor of 16) [8]. The convolutional layer is optimized to minimize task loss and do not explicitly enforce anti-aliasing. Consequently, the process of patchification reduces the Nyquist frequency in each subband, and it potentially introduces aliasing. Aliasing degrades the learned representation and can cause outputs to become sensitive to small input phase shifts [11]–[13]. This can cause instability during training and reduce sample efficiency. A straightforward solution to this problem is to apply a low-pass anti-aliasing filter prior to downsampling. However, this approach remains ineffective because high-frequency components can contain critical information for specific tasks. This creates a fundamental dilemma: we must mitigate aliasing without discarding informative high-frequency content during the patchification stage.

We introduce Aliasing-aware Patch Embedding (AaPE), implemented via a Structured Bilateral Laplace Unit (SBLU) inspired by structured state-space models (SSMs) [14], [15]. SBLU performs adaptive frequency analysis over spectrogram subbands, focusing on the ranges most susceptible to aliasing under patching. AaPE extracts aliasing-related frequency features and fuses them with standard patch tokens to explicitly compensate for aliasing. Specifically, we estimate aliasing factors using a band-limited complex sinusoidal kernel modulated by a two-sided exponential window. This design is motivated by the observation that two-sided exponential windows enhance the efficacy of gradient-based frequency feature extraction. The proposed kernel is derived through the extension of a structured SSM formulation for efficient frequency feature extraction, which is adapted to accommodate two-sided exponential windows. Expressiveness is enhanced through the dynamic estimation of the kernel’s decay and frequency parameters from the standard patch tokens, facilitating parallel extraction of useful frequency components across multiple subbands. As illustrated in Figure 1, the audio representation learning scheme with AaPE is outlined in summary. AaPE serves as a drop-in replacement for standard ViT patch embedding and is trained via teacher-student masked modeling in SSL. Masked prediction requires the inference of content that is contingent on aliasing-prone bands, resulting in the model’s learning of finer-grained features in comparison to conventional approaches. Furthermore, a multi-mask strategy combined with a contrastive regularization ensures consistency across diverse mask patterns, thereby facilitating training stability. We pre-train on AudioSet [16] and evaluate via fine-

¹Research & Development Center, Technology Division, Oki Electric Industry Co., Ltd., Saitama, Japan. ²Department of Data Science for Business Innovation, Chuo University, Tokyo, Japan. Kohei Yamamoto (e-mail: yamamoto833@oki.com) is a Ph.D. student at Chuo University and also with Oki Electric Industry Co., Ltd. Kosuke Okusa (e-mail: okusa@kc.chuo-u.ac.jp) is an Associate Professor at Chuo University, Tokyo, Japan.

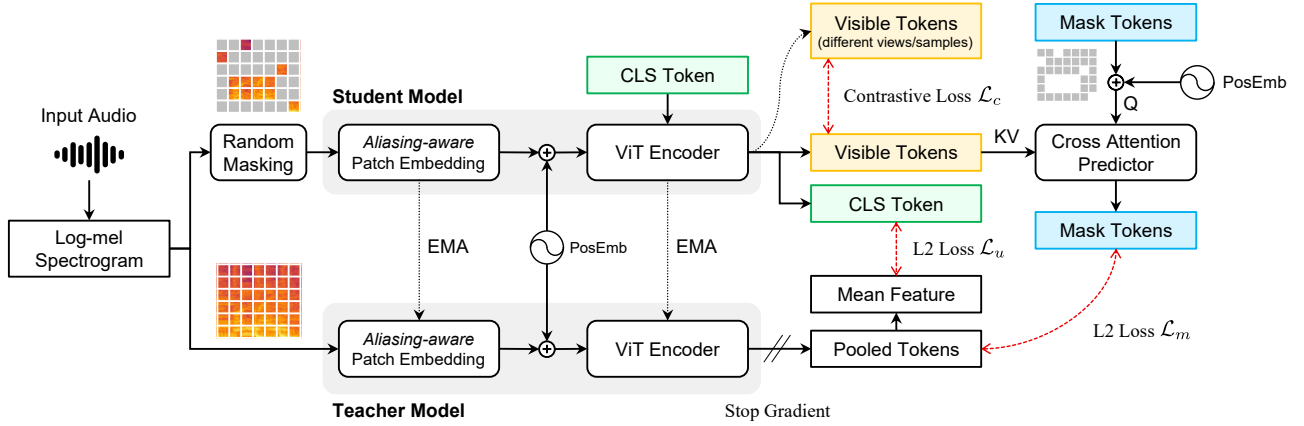


Fig. 1: **Overview of the Teacher-student Self-supervised Learning Scheme with AaPE.** Aliasing-aware Patch Embedding (AaPE) replaces the ViT patch embedding, performing dynamic subband frequency analysis to extract aliasing-aware features from aliasing-prone bands and fusing them with the standard patch tokens. The class (CLS) token predicts a global summary of the teacher outputs, while a cross-attention predictor performs masked prediction of the teacher’s layer-wise pooled tokens at masked positions. A multi-mask contrastive consistency regularization pulls together masked views of the same input and pushes apart views from different inputs. PosEmb denotes absolute positional embeddings [9].

tuning and linear probing across a range of downstream tasks, including environmental sounds, speech commands, musical instrument families, urban scenes, and acted emotions. Our results demonstrate state-of-the-art performance on certain benchmarks and competitive results on others.

Main contributions. The contributions of this study are as follows:

- Introduce Aliasing-aware Patch Embedding (AaPE), a drop-in ViT patch embedding that augments standard embeddings with aliasing-aware frequency features, to mitigate the effects of aliasing without discarding informative high-frequency content.
- Derive the Structured Bilateral Laplace Unit (SBLU) from a structured SSM formulation extended to two-sided exponential windows, yielding an efficient, differentiable, and gradient-friendly frequency feature extractor with dynamic per-subband parameterization.
- Present a self-supervised learning framework that integrates masked teacher-student prediction with a multi-mask contrastive regularization, enforcing cross-mask consistency, and improving training stability.
- Provide extensive experiments by pre-training on AudioSet and evaluating across multiple downstream tasks under fine-tuning and linear probing, indicating state-of-the-art results on certain datasets (e.g., AudioSet-20K [16], ESC-50 [17], UrbanSound8K [18], NSynth [19]) and competitive performance on others (e.g., AudioSet-2M [16], Speech Commands V2 [20], CREMA-D [21])

II. RELATED WORK

A. Audio Representation Learning

Audio representation learning can be broadly categorized into two families: time-domain (waveform) methods and time-frequency (spectrogram) methods. In both families, masked audio modeling (MAM) has become mainstream. The input is split into patches, a random subset is masked, and the model reconstructs these regions from visible patches to learn semantic features without labels.

Spectrogram-based SSL. This line of work applies MAM to spectrograms derived from audio. For instance, SSAST [5], MaskSpec [22], AudioMAE [3], and MAE-AST [4] introduce self-supervised learning based on spectrogram reconstruction within the Audio Spectrogram Transformer (AST [8]) framework. Conversely, BEATs [23] predicts discrete labels at the patch level and relies on teacher-model distillation rather than spectrogram reconstruction. A complementary direction employs self-distillation with an exponential moving average (EMA) teacher formed from the student’s parameters and minimizes the prediction error between student outputs and teacher latent features. This approach can be integrated within the MAM framework. For instance, ATST [6] feeds augmented visible patches to the student while the EMA teacher receives non-augmented inputs; M2D [7] additionally masks the teacher and enforces mutually exclusive masking patterns between student and teacher; ASiT [24] jointly learns spectrogram reconstruction and contrastive teacher-student distillation; EAT [25] introduces an utterance-level loss that aligns the encoder’s class token with an aggregation of teacher features; and ASDA [26] incorporates differential attention within the transformer encoder under the EAT framework. Finally, SSLAM [27] adds a loss that brings latent features of spectrogram mixtures closer to the mean of the corresponding un-mixed features. These models achieve strong results across diverse audio tasks; however, they typically assume aggressive compression of temporal resolution (via transform and patching), leaving aliasing-induced information loss unresolved.

Temporal-based SSL. wav2vec 2.0 [28] and HuBERT [29] extract features from raw waveforms using multiple convolutional layers and then apply MAM or related objectives in the latent space. As downsampling is applied progressively, aliasing is mitigated relative to spectrogram patching. However, convolutional stacks consist of learned filters without explicit anti-aliasing constraints, thus there is no guarantee they approximate ideal low-pass behavior, and aliasing cannot be fully avoided.

B. Temporal Modeling in Audio

State-space Models (SSMs). S4 [14] and S4D [15], rooted in continuous-time systems theory, unify properties of RNNs and CNNs and are effective for modeling long sequences. They estimate two linear maps alongside parameters controlling the decay and frequency of damping sinusoids. Mamba [30] extends S4D with a selective mechanism, making those linear maps and certain parameters (including decay and sampling period) input-dependent. Our work is inspired by the continuous-time signal-analysis perspective underlying S4. In contrast to S4 and Mamba which target general sequence modeling, our approach aims to analyze aliasing bands in spectrogram subband signals. Furthermore, we adopt input dependence in the spirit of Mamba; however, in this case, only the decay and frequency are conditioned on the input.

Learnable Frontends. LEAF [31], EfficientLEAF [32], and MuReNN [33] replace mel-filterbanks by applying Gabor filters to raw waveforms, with trainable center frequency and window width. Our approach similarly employs learnable kernels with trainable frequency and window width but operates on spectrogram subbands and is inspired by state-space modeling. Prior work has reported that frequency parameters in such learnable frontends are sensitive to initialization and exhibit limited drift after training [34]. Therefore, we hypothesize that vanishing gradients induced by Gaussian windows contribute to this effect and claim that adopting a two-sided exponential window alleviates the gradient-vanishing problem.

Anti-aliasing CNNs. Applying a low-pass filter before max pooling or strided convolution effectively enhances shift invariance by removing high-frequency content that could cause aliasing upon downsampling [11]–[13]. However, in audio analysis this fixed low-pass strategy can be suboptimal, because high-frequency components often carry salient information (e.g., transients and onsets). A uniform low-pass filter may suppress useful signal components together with noise. By contrast, our approach selectively extracts high-frequency information that patching could otherwise discard, reducing information loss.

III. METHODOLOGY

A. Preliminaries

Masked Autoencoder (MAE). In the audio domain, AudioMAE [3] patchifies an $F \times T$ log-mel spectrogram into non-overlapping $P_{\text{freq}} \times P_{\text{time}}$ patches. Here, P_{freq} and P_{time} denote the patch sizes along the frequency and time directions, respectively. Each patch is linearly projected, producing $N_{\text{patch}} = FT/(P_{\text{freq}}P_{\text{time}})$ patch tokens $\mathbf{x}_i \in \mathbb{R}^D$ ($i = 1, 2, \dots, N_{\text{patch}}$). It randomly masks a subset of patches, partitioning the patch set $\mathcal{X} = \{\mathbf{x}_1, \mathbf{x}_2, \dots, \mathbf{x}_{N_{\text{patch}}}\}$ into visible and masked subsets \mathcal{X}_{vis} and $\mathcal{X}_{\text{mask}}$ (i.e., $\mathcal{X}_{\text{vis}} \cup \mathcal{X}_{\text{mask}} = \mathcal{X}$ and $\mathcal{X}_{\text{vis}} \cap \mathcal{X}_{\text{mask}} = \emptyset$). The encoder consumes the visible patch tokens with positional embeddings and produces a set of output visible tokens \mathcal{Z}_{vis} . The predictor forms a length- N_{patch} sequence $\{\tilde{\mathbf{x}}_i\}$ by placing the encoder output at each visible index and a learnable mask token $\mathbf{m} \in \mathbb{R}^D$ at each masked index, followed by adding positional embeddings and reconstructing the original content at masked locations: $\tilde{\mathbf{x}}_i = \mathbf{z}_i \cdot \mathbb{I}(\mathbf{x}_i \in \mathcal{X}_{\text{vis}}) + \mathbf{m} \cdot \mathbb{I}(\mathbf{x}_i \in \mathcal{X}_{\text{mask}})$,

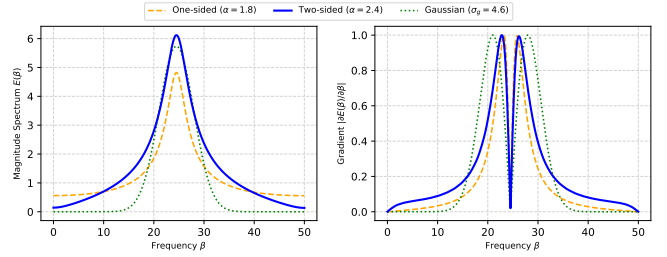


Fig. 2: **Spectra and Gradient Magnitudes for Various Window Functions.** The two-sided window sustains usable gradients over wider frequency offsets, while one-sided and Gaussian windows suffer rapid off-target vanishing; this supports our choice of a two-sided exponential window in SBLU for stable subband-wise estimation in aliasing-prone bands. The window parameters α and σ_g are normalized so that the peak gradient magnitude equals 1.0.

where \mathbf{z}_i denotes the encoder output aligned to the original index i when \mathbf{x}_i is visible. After pre-training, only the encoder is employed for downstream tasks. Recent work on audio MAE variants often favors self-distillation (teacher-student) over reconstruction [6], [7], [25], using an EMA teacher and training the encoder (student) to match the teacher’s outputs.

Structured SSMs. Structured SSMs define learnable matrices $\mathbf{A} \in \mathbb{R}^{H \times H}$, $\mathbf{B} \in \mathbb{R}^{H \times F}$, and $\mathbf{C} \in \mathbb{R}^{C \times H}$, and model the continuous-time system $\frac{d}{dt}\mathbf{h}(t) = \mathbf{A}\mathbf{h}(t) + \mathbf{B}\mathbf{u}(t)$ and $\mathbf{y}(t) = \mathbf{C}\mathbf{h}(t)$, which maps the input $\mathbf{u}(t) \in \mathbb{R}^F$ at time t to the output $\mathbf{y}(t) \in \mathbb{R}^C$ via the latent state $\mathbf{h}(t) \in \mathbb{R}^H$ [14]. Applying zero-order-hold (ZOH) discretization and the diagonalization $\mathbf{A} = \mathbf{P}^{-1}\mathbf{\Lambda}\mathbf{P}$ yields the discrete-time system [15]

$$\mathbf{y}[n] = \overline{\mathbf{C}}\mathbf{\Lambda}^{-1} (e^{\Delta\mathbf{\Lambda}} - \mathbf{I}) \sum_{k=0}^n e^{\Delta\mathbf{\Lambda}(k-n)} \overline{\mathbf{B}}\mathbf{u}[k], \quad (1)$$

where $\mathbf{h}(0) = 0$, the sampling period is $\Delta \in \mathbb{R}$, the time index is $n = 0, 1, \dots, N_{\text{time}} - 1$, $\overline{\mathbf{B}} = \mathbf{P}^{-1}\mathbf{B}$, $\overline{\mathbf{C}} = \mathbf{C}\mathbf{P}^{-1}$, and $\mathbf{y}[n] = \mathbf{y}(n\Delta)$ denotes the discrete-time output. The complex diagonal matrix $\mathbf{\Lambda} = \text{diag}(\lambda_1, \dots, \lambda_H) \in \mathbb{C}^{H \times H}$ has entries $\lambda_i = \alpha_i + j\beta_i$ (with j denoting the imaginary unit), whose real and imaginary parts can be interpreted as a decay α_i and a frequency β_i (by multiplying 2π), respectively. Consequently, the above expression is a causal, one-sided convolution along time with a complex sinusoidal kernel modulated by an exponential window. For convenience, we write α, β in place of α_i, β_i when the index is clear.

B. Structured Bilateral Laplace Unit (SBLU)

Motivation. We leverage the structured SSMs to extract frequency-focused features from the subband signals of the log-mel spectrogram, by constraining the frequency parameter β to the frequency band that contains aliasing artifacts. For stable gradient-based learning of β per subband, the gradient of the convolution output with respect to β must not vanish. Because this gradient is governed by the window’s frequency response, the one-sided exponential window in Eq. (1) suffers from gradient vanishing. Define a local spectrum at β by $E(\beta) = \left| \sum_{k=0}^{N_w-1} w[k] x[k] e^{-j2\pi\beta k\Delta} \right|$, for an arbitrary input $x[k]$ and window $w[k]$ of length N_w . For a single-tone

input $x[k] = e^{j2\pi\omega_0 k\Delta}$, we obtain $E(\beta) = |W(\omega_\delta)|$, where $\omega_\delta = \omega_0 - \beta$ and $W(\omega) = \sum_k w[k]e^{j2\pi\omega k\Delta}$ is the window's frequency response. Thus, $\partial E(\beta)/\partial\beta = -d|W(\omega_\delta)|/d\omega_\delta$, and the gradient magnitude follows the slope of the window's spectral envelope. Figure 2 shows spectra and gradients for a one-sided exponential $w[k] = \exp(-\alpha(N_w - 1 - k))$ [35], a two-sided exponential $w[k] = \exp(-\alpha|(N_w - 1)/2 - k|)$, and a Gaussian $w[k] \propto \exp(-((N_w - 1)/2 - k)^2/(2\sigma_g^2))$ (as in [31], [33]) with $\Delta = 0.01$, $N_w = 127$, and $\omega_0 = 24.5$. One-sided exponentials have high average sidelobes owing to edge discontinuity, yet their gradients diminish rapidly away from the target. Gaussians yield large gradients near the target but very fast sidelobe decay, causing abrupt gradient vanishing. Two-sided exponentials maintain usable gradient magnitudes across a wider frequency range.

Formulation. Based on these observations, we introduce the Structured Bilateral Laplace Unit (SBLU), replacing the one-sided window in Eq. (1) with a two-sided exponential to reduce gradient vanishing. Let $\mathbf{u}(t)$ be the subband signals of a log-mel spectrogram with F mel bands, and extend Eq. (1) to a complex sinusoidal kernel with a two-sided exponential window:

$$\mathbf{y}[n] = 2\bar{\mathbf{C}}\bar{\mathbf{A}}^{-1} \sinh\left(\frac{\Delta\mathbf{A}}{2}\right) \sum_{k=0}^{K-1} e^{-\Delta\mathbf{A}|k-c|} \bar{\mathbf{B}}\mathbf{u}[n+k-c] \quad (2)$$

where the kernel size $K > 1$ is odd and $c = (K - 1)/2$ is the center index (derivation in Appendix A). This operation is analogous to a discrete bilateral Laplace transform. The two-sided window sacrifices strict causality but gains locality, thus we implement SBLU as a centered sliding-window convolution. As the initial phase depends on the window's time position, phase variability arises; thus, we assume the magnitude after convolution to suppress phase variation:

$$\mathbf{y}[n] = 2\bar{\mathbf{C}}\bar{\mathbf{A}}^{-1} \left| \sum_{k=0}^{K-1} e^{-\Delta\mathbf{A}|k-c|} \bar{\mathbf{B}}\mathbf{u}[n+k-c] \right|, \quad (3)$$

$$\gamma_i = \sqrt{\frac{\cosh^2(\frac{\Delta\alpha_i}{2}) - \cos^2(\frac{\Delta\beta_i}{2})}{\alpha_i^2 + \beta_i^2}} \quad (4)$$

with $\mathbf{\Gamma} = \text{diag}(\gamma_1, \dots, \gamma_H)$ (derivation in Appendix B). As the final output is real-valued, we treat $\bar{\mathbf{B}}$ and $\bar{\mathbf{C}}$ as real trainable matrices, while the convolution itself proceeds in the complex domain.

Band focusing and stability constraints. We target aliased components by restricting the frequency to $\beta \in [\beta_{\min}, \beta_{\max}]$, where the lower bound is the post-patching Nyquist frequency $\beta_{\min} = \pi/(\Delta P_{\text{time}})$ and the upper bound is the pre-patching Nyquist frequency $\beta_{\max} = \pi/\Delta$. Window-edge discontinuity causes ringing in the side lobes of the window's spectral envelope. The gradient direction for β depends on the local slope of this envelope, and the ringing flips the slope across nearby frequencies. Consequently, gradient descent on β becomes unstable. Therefore, we impose a positive lower bound on the decay α by requiring edge attenuation $e^{-\Delta\alpha(K-1)/2} \leq \epsilon$, yielding $\alpha_{\min} = -\frac{2\log(\epsilon)}{\Delta(K-1)}$. We enforce $\alpha \geq \alpha_{\min}$ and $\beta \in [\beta_{\min}, \beta_{\max}]$.

C. Aliasing-aware Patch Embedding (AaPE)

Figure 3 illustrates the architecture of AaPE. We extract high-frequency subband features using SBLU and fuse them with the standard patch tokens to compensate for aliasing artifacts. To increase expressivity while preserving the structure of patch tokens, we make the learnable decay and frequency parameters in SBLU \mathbf{A} input-dependent. This yields a non-stationary kernel that adapts to local amplitude and frequency modulations and other input variations, improving modeling flexibility. Concretely, our pipeline comprises three components: (1) Lambda Encoder, which adaptively estimates decay and frequency from patch tokens; (2) Adaptive SBLU, which performs frequency analysis conditioned on the estimated parameters; and (3) Patch Fusion, fusing the resulting frequency features with the original patch tokens.

Lambda Encoder. We start from the log-mel spectrogram $\mathbf{X}_{\text{mel}} \in \mathbb{R}^{F \times T}$. Using non-overlapping patches of size $P_{\text{freq}} \times P_{\text{time}}$ (assuming F and T are divisible by P_{freq} and P_{time}), we obtain $\tilde{F} = F/P_{\text{freq}}$ frequency patches and $\tilde{T} = T/P_{\text{time}}$ temporal patches. A 2D convolution produces a standard patch embedding $\mathbf{X}_{\text{spec}} \in \mathbb{R}^{D \times \tilde{F} \times \tilde{T}}$. We add absolute positional embeddings [9] to \mathbf{X}_{spec} and estimate input-dependent parameters $\mathbf{\Lambda}_{\text{alias}} \in \mathbb{C}^{H \times T}$ over the original temporal grid using the Lambda Encoder. Internally, we first reduce the embedding dimension of \mathbf{X}_{spec} from D to D/r via a linear projection, then apply L Transformer blocks; we employ a narrow-and-shallow configuration with $r = 6$ and $L = 3$ to improve throughput. The Transformer Block design (attention, number of heads, MLP ratio) is identical to the original ViT architecture [9]. Using Transformer Blocks is advantageous in MAE because computations over masked regions can be omitted. Subsequently, a second linear map projects the output to an embedding dimension of $2H/\tilde{F}$, matching the SBLU hidden dimension H . We split the output embeddings along the embedding dimension into two equal parts, interpreted as the real component α and the imaginary component β of the complex kernel parameter. We obtain a lower-bounded decay parameter by applying softplus and a shift: $\alpha_{\text{bound}} = \text{softplus}(\alpha) + \alpha_{\min}$. For the frequency, we bound it to a target interval by applying a sigmoid followed by an affine mapping: $\beta_{\text{bound}} = (\beta_{\max} - \beta_{\min})\sigma(\beta) + \beta_{\min}$. We construct a complex-valued parameter tensor by employing the bounded decay as the real part and the bounded frequency as the imaginary part. To align the parameters with the original temporal resolution while maintaining patch-level, we replicate each time-patch entry P_{time} times along the temporal axis such that $\tilde{T} \rightarrow T$, yielding a tensor of shape $\mathbb{C}^{\frac{H}{\tilde{F}} \times \tilde{F} \times T}$. Finally, we collapse the frequency-patch axis into the hidden dimension H by reshaping $\mathbb{C}^{\frac{H}{\tilde{F}} \times \tilde{F} \times T} \rightarrow \mathbb{C}^{H \times T}$ to obtain $\mathbf{\Lambda}_{\text{alias}}$.

Adaptive SBLU. Given \mathbf{X}_{mel} and $\mathbf{\Lambda}_{\text{alias}}$, the module produces an aliasing-focused representation $\mathbf{X}_{\text{alias}} \in \mathbb{R}^{\tilde{C} \times \tilde{F} \times \tilde{T}}$, where $\tilde{C} = C/\tilde{F}$. To emphasize aliasing bands, we apply a zero-phase high-pass filter along the time axis, implemented via forward-backward filtering of a 63-tap Hamming-window FIR, with the cutoff set to the Nyquist frequency of the post-patching sampling rate. We apply the linear map $\bar{\mathbf{B}}$. In SBLU, the linear maps $\bar{\mathbf{B}} \in \mathbb{R}^{H \times F}$ and $\bar{\mathbf{C}} \in \mathbb{R}^{C \times H}$ act as point-

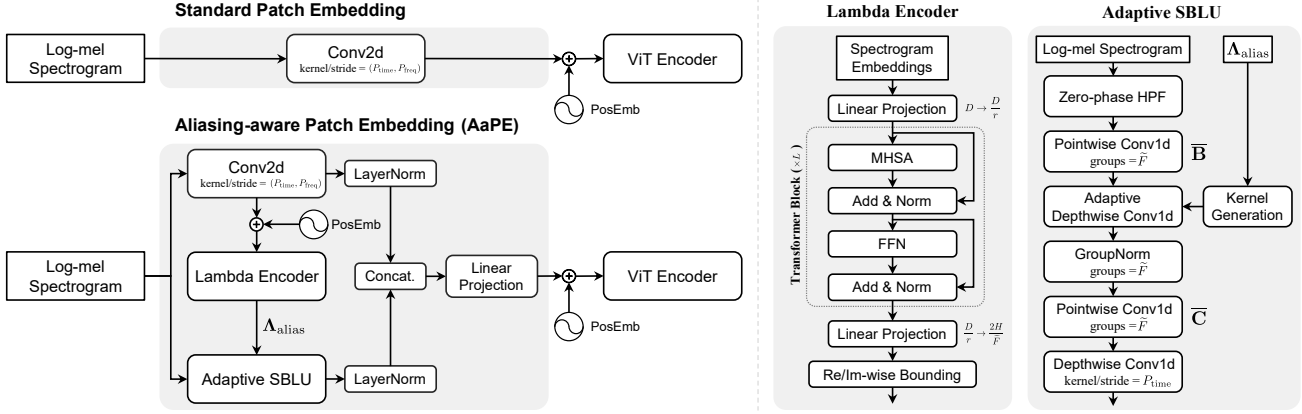


Fig. 3: **Architecture of the Aliasing-aware Patch Embedding (AaPE)**. AaPE augments the standard ViT patch embedding with aliasing-aware features via three components: (1) Lambda Encoder—takes log-mel spectrogram patches and estimates input-dependent complex kernel parameters Λ_{alias} with decay α and frequency β per subband using a narrow-and-shallow Transformer and linear projections; (2) Adaptive SBLU—emphasizes aliasing-prone bands with a zero-phase high-pass filter, generates bilateral complex sinusoidal kernels from Λ_{alias} , and performs memory-efficient adaptive depthwise convolution with grouped pointwise projections to produce an aliasing-focused high-frequency representation; (3) Patch Fusion—independently normalizes and concatenates the standard and aliasing-focused features, then linearly projects to D dimensions to yield the final aliasing-aware patch embedding fed to the ViT encoder.

wise convolutions; to preserve independence across frequency patches, we implement both as grouped convolutions with \tilde{F} groups. Next, we generate complex sinusoidal kernels from Λ_{alias} and window them with a two-sided exponential. We then apply an adaptive depthwise convolution along the time axis with stride 1 and symmetric zero padding of $(K-1)/2$ samples per side. Pre-generating a kernel for every time frame is memory-prohibitive for long kernels, thus we fuse on-the-fly kernel generation with convolution, leveraging that the sinusoid is parameterized only by decay α and frequency β . During backpropagation, we obtained that the gradient terms exhibit a coupling that allows reuse of the same convolution results for two parameter-gradient pairs (details and exact pairings are provided in Appendix C), reducing the number of convolution evaluations. We apply \tilde{C} , followed by GroupNorm for training stability, using \tilde{F} groups to maintain frequency-patch independence. Time-only patchification is performed by a depthwise convolution along the temporal axis (i.e., $\mathbb{R}^{C \times T} \rightarrow \mathbb{R}^{C \times \tilde{T}}$). Finally, we reshape from $\mathbb{R}^{C \times \tilde{T}}$ to $\mathbb{R}^{\tilde{C} \times \tilde{F} \times \tilde{T}}$ to obtain the aliasing-focused representation $\mathbf{X}_{\text{alias}}$.

Patch Fusion. After independently normalizing \mathbf{X}_{spec} and $\mathbf{X}_{\text{alias}}$, we concatenate them and apply a linear projection $f_{\text{fuse}} : \mathbb{R}^{(D+\tilde{C}) \times \tilde{F} \times \tilde{T}} \rightarrow \mathbb{R}^{D \times \tilde{F} \times \tilde{T}}$ to produce the final aliasing-aware patch tokens $\mathbf{X}_{\text{fused}} \in \mathbb{R}^{D \times \tilde{F} \times \tilde{T}}$, which is fed to the ViT encoder.

D. Predictor and Pre-training Objectives

As shown in Fig. 1, we learn semantic representations from AaPE and the ViT encoder using a teacher-student framework following EAT [25]. The teacher parameters are updated as an EMA of the student, stop-gradient is applied to teacher outputs, and the predictor operates only on the student side. Our predictor is a stack of three cross-attention blocks [36] to facilitate training, each comprising multi-head cross-attention and a position-wise MLP. During prediction, mask tokens act as queries and attend only to visible tokens (used as keys and values); there is no attention among mask tokens. This design enables efficient training and demonstrates that cross-

attention is effective in the original MAE framework [36] as well as within a teacher-student framework. We optimize three complementary objectives: a masked-prediction objective, an utterance-level alignment objective, and a contrastive regularization term. We generate M masked views per input sample during pre-training. The training framework and masking strategy are detailed in Section IV-B.

Masked Prediction Objective. The masking loss \mathcal{L}_m encourages reconstruction of latent patch representations by minimizing the L2 distance between the predictor’s outputs on mask tokens and teacher-provided targets. Consistent with EAT [25], the teacher omits a class token. We construct the teacher pooled tokens as follows. In each teacher layer, instance normalization is applied per token and per sample across the embedding dimension, without learnable affine parameters. These normalized tokens are then averaged across layers, followed by layer normalization across the embedding dimension, also without learnable affine parameters. The loss \mathcal{L}_m is computed only on the masked tokens, as the cross-attention predictor uses them as queries.

Utterance-Level Objective. The utterance-level loss \mathcal{L}_u aligns the student’s global representation by minimizing the L2 distance between the encoder’s class token and the teacher’s utterance-level target, computed as the mean over the teacher pooled tokens, following [25].

Contrastive Regularization. Inspired by SimCLR [37], we introduce a contrastive loss to promote stability and robustness across masked views of the same input sample. For each view, the student’s visible tokens are averaged to a single vector, which is fed to a two-layer MLP with hidden dimension equal to half the embedding dimension and GELU activation, followed by a linear output layer; the MLP output is the embedding $\tilde{\mathbf{z}}_i$. All embeddings are L2-normalized before similarity computation, allowing the dot product to represent cosine similarity. The temperature is fixed to $\tau = 0.2$. For each $\tilde{\mathbf{z}}_i \in \tilde{\mathcal{Z}}_{\text{vis}}$, all pairwise combinations of different masks (views) from the same sample (i.e., ${}_M C_2$) are treated as positives, and embeddings from other samples in the batch serve as negatives.

The InfoNCE-based contrastive loss [37] is

$$\mathcal{L}_c = -\frac{1}{N_{\text{vis}}} \sum_{i=1}^{N_{\text{vis}}} \sum_{p \in \mathcal{P}(i)} \log \frac{\exp(\tilde{\mathbf{z}}_i^\top \tilde{\mathbf{z}}_p / \tau)}{\sum_{a \in \mathcal{A}(i)} \exp(\tilde{\mathbf{z}}_i^\top \tilde{\mathbf{z}}_a / \tau)}, \quad (5)$$

where $N_{\text{vis}} = |\tilde{\mathcal{Z}}_{\text{vis}}|$ is the total number of embeddings across all views in the batch, $\mathcal{P}(i)$ indexes positives for $\tilde{\mathbf{z}}_i$ (same input, different masks), and $\mathcal{A}(i)$ includes $\mathcal{P}(i)$ and all embeddings from other inputs; the anchor $\tilde{\mathbf{z}}_i$ is excluded, and views of the same input that are not in $\mathcal{P}(i)$ are excluded from the denominator.

The final objective is as follows:

$$\mathcal{L}_{\text{total}} = \mathcal{L}_m + \mathcal{L}_u + \eta \mathcal{L}_c, \quad (6)$$

with a regularization loss weight η . Following [25], we fix unit weights for \mathcal{L}_m and \mathcal{L}_u and vary only the contrastive coefficient in ablations (see Section IV-D).

IV. EXPERIMENTS

A. Datasets

Here, we evaluate on six datasets across seven evaluation settings: AudioSet in two settings (AS-2M and AS-20K) and five single-label benchmarks (ESC-50, SCV2, NSynth, US8K, CREMA-D), covering environmental sounds, speech commands, musical instrument families, urban scenes, and acted emotions.

- **AudioSet (AS-2M, AS-20K)** [16] is a large-scale multi-label dataset of 10-second YouTube clips covering 527 classes. The released training split comprises 2,042,985 unbalanced clips and a 22,176 balanced subset; the evaluation split has 20,383 clips. Owing to missing videos, we retain approximately 1.96M unbalanced, approximately 21k balanced, and approximately 19k evaluation clips. For AS-2M, supervised fine-tuning uses class-balanced sampling (weighted sampling size is 200K). For AS-20K, we fine-tune on the balanced approximately 20k subset (pre-trained on full AS-2M) and report mAP.
- **ESC-50** [17] is a single-label environmental sound dataset with 2,000 five-second clips across 50 classes. We follow the official 5-fold protocol and report mean accuracy across folds.
- **Speech Commands V2 (SCV2)** [20] is a single-label keyword spotting dataset comprising 105,829 one-second clips across 35 classes. With the official split (84,843 train, 9,981 validation, 11,005 test), we fine-tune the AS-2M-pre-trained model and report accuracy.
- **NSynth** [19] is a single-label instrument family classification dataset with 305,979 four-second clips across 11 classes. With the official split (289,205 train, 12,678 validation, 4,096 test), we perform linear probing following [7].
- **UrbanSound8K (US8K)** [18] is a single-label urban sound dataset containing 8,732 clips up to four seconds across 10 classes. We conduct linear probing with 10-fold cross-validation using the official folds and report mean accuracy.

Hyperparams.	Pre-training	Fine-tuning			
	AS-2M	AS-2M	AS-20K	ESC-50	SCV2
Optimizer	AdamW [38] with $\beta_1 = 0.9, \beta_2 = 0.95$				
LR schedule	Cosine Annealing [39] with linear warm-up				
Peak LR	5.0×10^{-4}		5.0×10^{-5}		
Minimum LR	0.0	10^{-6}	10^{-6}	10^{-7}	10^{-7}
Layer decay [40]	N/A	0.70	0.70	0.65	0.75
Weight decay	0.05	0.05	0.05	0.05	0.05
Training steps	600K	300K	40K	8K	160K
Warm-up steps	80K	30K	4K	800	16K
Batch size	512	128	128	128	128
# of GPUs	4	4	4	1	1
Mixup [41]	0.0	0.8	0.8	0.0	0.8
Drop path [42]	0.0	0.1	0.1	0.1	0.1

TABLE I: **Hyperparameters for Pre-training and Fine-tuning.** Batch size means the total batch size for the multi-GPU training.

Hyperparams.	Linear Probing		
	US8K	NSynth	CREMA-D
Optimizer	Adam with $\beta_1 = 0.9, \beta_2 = 0.999$		
LR schedule	Cosine Annealing [39]		
Peak LR	3.0×10^{-3}	1.0×10^{-3}	5.0×10^{-4}
Minimum LR	0.0	0.0	0.0
Weight decay	0.0	0.0	0.0
Training steps	8K	50K	50K
Batch size	128	512	16
# of GPUs	1	1	1

TABLE II: **Hyperparameters for Linear Probing.**

- **CREMA-D** [21] is a single-label emotion recognition dataset with 7,438 utterances of approximately 2.5 s across 6 classes. With the split (5,155 train, 732 validation, 1,551 test) following [7], we perform linear probing with the AS-2M-pre-trained model.

B. Training Setup

We summarize the protocols for pre-training, fine-tuning, and linear probing (also referred to as linear evaluation) below. The hyperparameters used for pre-training and fine-tuning are listed in Table I, while those for linear probing are shown in Table II. All fine-tuning or linear probing experiments use a model pre-trained on AS-2M without label information. Unless otherwise noted, all audio is resampled to 16 kHz, and log-mel spectrograms are computed with a 400-sample Hann window, 160-sample hop, 128 mel-bins ($F = 128$), and an FFT size of 1,024. For SBLU, we set the kernel size $K = 63$, the step size $\Delta = 0.01$, the patch size $P_{\text{time}} = P_{\text{freq}} = 16$, the SBLU hidden dimension $H = 128$, the output dimension $C = 1,024$ and the window attenuation threshold $\epsilon = 0.01$. The contrastive regularization loss weight η is set to 0.1 by default. Log-mel spectrograms are standardized using mean -7.1 and standard deviation 4.1. Training is conducted on NVIDIA H100-80GB GPUs.

Pre-training Setup. We employ a teacher-student framework to learn representations from the acoustic patch sequence produced by AaPE. The student encoder is a 12-layer Vision Transformer [9]. The predictor consists of the 3 cross-attention blocks as in CrossMAE [36], with hidden size 512 and 16 heads. Queries are randomly selected from masked tokens; we use 75% of the masked tokens as queries to facilitate training as in [36]. We apply inverse block masking [25]

with an 80% token mask ratio and a multi-mask scheme with $M = 4$ masks (views) per input; all M views are included in the same batch. For each view, we sample a block size uniformly from $\{3 \times 8, 4 \times 6, 5 \times 5\}$ in (frequency \times time) patches; the remaining tokens required to reach the 80% mask ratio are selected via non-block random masking. Block locations and the residual random masks are sampled independently for each of the M views. The teacher branch is stop-gradient and updated via an EMA of the student using a cosine momentum schedule identical to [2]. Specifically, $\theta_{\text{teacher}}^{(m)} \leftarrow \xi^{(m)} \theta_{\text{teacher}}^{(m-1)} + (1 - \xi^{(m)}) \theta_{\text{student}}^{(m)}$ where m is the iteration step and $\xi^{(m)}$ increases from 0.994 to 1.0 over the maximum iterations as in [2]. Teacher signals (pooled tokens and their mean-pooled utterance target) are formed using functional instance and layer normalization without learnable affine parameters. AS-2M clips are 10 s; for efficiency, we randomly crop 6-second segments and set the log-mel spectrogram length to 608 time frames by truncation or zero-padding, following prior work [6], [7]. We utilize 2D absolute positional embedding (time-frequency) as in [3]. For downstream inputs shorter than the pre-training length, embeddings are truncated; for longer inputs, they are extended via linear interpolation along the time axis, leaving the frequency axis unchanged.

Fine-tuning Setup. Following [25], we append a Layer-Norm and a linear classification head on the class token, optimizing all parameters end-to-end with a small learning rate. We adopt layer-wise learning-rate decay (Layer decay [40]) as in [6], [25], assigning smaller learning rates to earlier layers. For data augmentation, Mixup [41] and SpecAugment [43] are applied, with the mask size of one-fifth the input spectrogram size; no data augmentation is used for ESC-50. During fine-tuning except for ESC-50, an EMA of model weights with decay 0.995 is maintained for stable inference. Loss functions follow the task: multi-label datasets use BCE-with-logits; single-label datasets use cross-entropy unless Mixup is applied, in which case we use BCE.

Linear Probing Setup. In this setup, we concatenate the class token with the average-pooled patch token to obtain the final feature representation. We freeze the pre-trained encoder and train only a linear classifier mapping the class token to the number of classes. As in [6], no data augmentation is used for linear probing. The features obtained from the pre-trained encoder are collectively standardized, immediately prior to being input to the linear classifier, using pre-computed statistics over the entire training set.

All results are averaged over three random seeds per experiment. For all evaluation scores, we report the best result achieved within the specified number of training steps.

C. Evaluation Results

The effectiveness of AaPE on standard benchmarks is evaluated against state-of-the-art baselines.

Performance for Fine-tuning. Table III reports results for fine-tuning models pre-trained in a self-supervised manner on AudioSet across four benchmarks (AS-2M, AS-20K, ESC-50, SCV2). On AS-2M, AaPE achieves 49.8%, surpassing prior state-of-the-art methods except SSLAM [27]. SSLAM’s

Model	#Params.	AS-2M mAP(%)	AS-20K mAP(%)	ESC-50 Acc(%)	SCV2 Acc(%)
MaskSpec [22]	86M	47.1	32.3	89.6	97.7
data2vec [44]	94M	-	34.5	-	-
Audio-MAE [3]	86M	47.3	37.1	94.1	98.3
M2D/0.7 [7]	86M	47.9	38.6	96.0	98.4
ASiT [24]	86M	48.0	38.3	95.6	98.9
BEATs _{iter3} [23]	90M	48.0	38.3	95.6	98.3
ATST-Frame [6]	86M	48.0	39.0	-	98.1
EAT [25]	88M	48.6	40.2	95.9	98.3
ASDA [26]	93M	49.0	41.5	96.1	98.3
SSLAM [27]	88M	50.2	40.9	96.2	98.1
AaPE (ours)	87M	49.8	41.9	97.5	97.9

TABLE III: Performance Comparison on Fine-tuning.

gains typically derive from Mixup-based pre-training augmentation and its associated loss, whereas our contribution is architectural—an improved patch embedding. These approaches are orthogonal and non-exclusive; combining AaPE with SSLAM could yield additive gains and is a promising direction for future work. Beyond AS-2M, AaPE attains the best results on AS-20K (41.9% mAP, +0.4 percentage points over ASDA [26]) and ESC-50 (97.5% Acc., +1.3 percentage points over SSLAM), and remains competitive on SCV2 (97.9% Acc.), slightly below SSLAM (98.1%) and ASiT (98.9%; −1.0 percentage points). We hypothesize that, because SCV2 consists of 1-second signals, AaPE may not fully leverage frequency cues within such short contexts.

Performance for Linear Probing. Table IV reports linear probing results on three benchmarks (US8K, NSynth, CREMA-D). On US8K, AaPE achieves 89.7%, exceeding the state-of-the-art MATPAC [45] by +0.3 percentage points. On NSynth, AaPE attains 80.5%, outperforming ATST-Frame [6] and BEATs_{iter3} [23] by +4.6 percentage points. Instrumental sounds, with their periodic and quasi-stationary patterns, benefit from frequency-sensitive feature extraction via SBLU. By contrast, on CREMA-D, AaPE is 4.3 percentage points below M2D [7], suggesting that SBLU’s amplitude-modulation features are less effective for pitch-sensitive tasks such as emotional speech.

Model	#Params.	US8K Acc(%)	NSynth Acc(%)	CREMA-D Acc(%)
BEATs _{iter3} [23]	90M	84.8	75.9	64.7
ATST-Frame [6]	86M	85.8	75.9	72.3
M2D/0.7 [7]	86M	87.6	75.7	73.0
MATPAC/n10 [45]	86M	89.4	74.3	-
AaPE (ours)	87M	89.7	80.5	68.7

TABLE IV: Performance Comparison on Linear Probing.

Overall, AaPE delivers strong performance under both fine-tuning and linear probing, with pronounced gains on datasets where frequency structure is prominent.

D. Ablation Studies

We assess how each major component of the proposed method contributes to the final performance.

Patch Embedding and Contrastive Weight. Table V reports fine-tuning results on AS-2M (mAP), AS-20K (mAP),

and ESC-50 (Acc), comparing the standard patch embedding (SPE) with our Aliasing-aware Patch Embedding (AaPE) under contrastive regularization weights $\eta \in \{0.001, 0.01, 0.1\}$. With SPE, $\eta = 0.01$ yields the best performance across all three datasets; increasing to $\eta = 0.1$ degrades performance, while too-weak regularization ($\eta = 0.001$) underperforms the best setting. With AaPE, performance consistently improves as the contrastive weight increases, and $\eta = 0.1$ achieves the best results on all datasets. At matched weights, AaPE improves mAP on AS-2M by +4.0, +0.3, and -0.3 percentage points at $\eta = 0.1, 0.01,$ and $0.001,$ respectively; on AS-20K, the gains are +6.3, +0.7, and +0.1 mAP points at the same η values, respectively; on ESC-50, AaPE improves accuracy by +3.9, +0.9, and +0.9 points at $\eta = 0.1, 0.01,$ and $0.001,$ respectively. These patterns indicate that AaPE more effectively mitigates aliasing and, in contrast to SPE, can exploit a stronger contrastive signal ($\eta = 0.1$) without over-regularization. Although AaPE increases patch-embedding parameters from 0.43M to 1.86M, the gains at matched weights suggest benefits beyond capacity alone.

PatchEmb. Type	Contrastive Loss weight η	#Params. (PatchEmb.)	AS-2M mAP(%)	AS-20K mAP(%)	ESC-50 Acc(%)
Standard	0.1	0.43M	45.8	35.6	93.6
Standard	0.01	0.43M	49.4	41.0	96.4
Standard	0.001	0.43M	48.6	38.6	95.1
Aliasing-aware	0.1	1.86M	49.8	41.9	97.5
Aliasing-aware	0.01	1.86M	49.7	41.7	97.3
Aliasing-aware	0.001	1.86M	48.3	38.7	96.0

TABLE V: **Ablation of Patch Embedding and Contrastive Regularization for Fine-tuning.** Gray-shaded row denotes the default configuration. Parameter counts reflect patch-embedding layer parameters only.

Adaptivity of SBLU. Within AaPE, SBLU extracts frequency features from each log-mel spectrogram patch. We introduce Adaptive SBLU, which estimates the kernel parameters (decay and frequency) per patch via the Lambda encoder (see Sec. III-C). In the non-adaptive ablation, these per-patch parameters are replaced with learnable parameters that are fixed across time patches. Table VI reports fine-tuning results under this ablation. Removing adaptivity consistently reduces performance across all datasets: mAP on AS-2M and AS-20K, and Acc on ESC-50 decrease by 0.1, 0.2, and 0.3, respectively. The adaptive variant increases the parameter count in the patch embedding module (1.86M vs 1.16M), yet the gains are stable across scales (AS-2M and AS-20K) and tasks (ESC-50), supporting the hypothesis that context-dependent estimation of aliasing-prone frequency bands improves downstream accuracy during fine-tuning. Overall, adaptivity provides small but consistent improvements at the cost of higher module

SBLU Adaptivity	#Params. (PatchEmb.)	AS-2M mAP(%)	AS-20K mAP(%)	ESC-50 Acc(%)
Non-adaptive	1.16M	49.7	41.7	97.2
Adaptive	1.86M	49.8	41.9	97.5

TABLE VI: **Ablation of SBLU Adaptivity for Fine-tuning.** Gray-shaded row denotes the default configuration. In the non-adaptive setting, the Lambda encoder is disabled and its frequency/decay parameters are learned as static, input-independent values.

complexity. When model size or latency is constrained, non-adaptive SBLU remains competitive and simplifies the patch embedding. Thus, SBLU itself is effective, with adaptivity serving as an optional enhancement that can be enabled when resources permit.

Kernel Size of SBLU. Table VII examines the effect of kernel size K in Adaptive SBLU, generating a complex sinusoidal kernel modulated by a two-sided exponential window, and reports FLOPs for the adaptive depthwise convolution only. Relative to the default $K = 63$, increasing K to 127 yields uniform +0.1 absolute improvements on AS-2M mAP, AS-20K mAP, and ESC-50 accuracy, while increasing compute from 4.90M to 9.86M FLOPs; decreasing K to 31 preserves mAP on AS-2M and AS-20K and reduces ESC-50 by -0.1, with 2.41M FLOPs. Overall, we observe a mild positive trend whereby broader receptive fields (larger K) tend to yield slightly higher scores across the three benchmarks.

Kernel size of SBLU	FLOPs	AS-2M mAP(%)	AS-20K mAP(%)	ESC-50 Acc(%)
$K = 31$	2.41M	49.8	41.9	97.4
$K = 63$	4.90M	49.8	41.9	97.5
$K = 127$	9.86M	49.9	42.0	97.6

TABLE VII: **Ablation of SBLU Kernel Size for Fine-tuning.** Gray-shaded row denotes the default configuration. FLOPs are computed only for the adaptive depthwise convolution within SBLU (forward pass only).

Predictor Architecture. In our method, the mask predictor is instantiated as a cross-attention module that uses the mask tokens as queries and visible tokens as keys/values. Table VIII reports fine-tuning results when replacing this predictor with the CNN used in prior work [25]–[27]. Although the cross-attention predictor has more parameters than the CNN, it delivers higher end-to-end throughput and essentially comparable downstream accuracy with small, consistent gains on two datasets. Relative to the CNN, throughput increases from 2.72 to 2.83 batches/sec, while the downstream differences are -0.1 mAP on AS-2M, +0.1 mAP on AS-20K, and +0.1 percentage points on ESC-50, respectively. We hypothesize two contributing factors: following [36], 25% of mask tokens are randomly dropped during training, reducing computation, and optimized attention implementations are employed. These observations suggest that cross-attention offers a favorable accuracy-efficiency trade-off for the mask predictor under our training setup.

Predictor Arch.	#Params. (Predictor)	Throughput (batch/sec)	AS-2M mAP(%)	AS-20K mAP(%)	ESC-50 Acc(%)
CNN	2.59M	2.72	49.9	41.8	97.4
CrossAttention	10.63M	2.83	49.8	41.9	97.5

TABLE VIII: **Ablation of Predictor Architecture for Fine-tuning.** Gray-shaded row denotes the default configuration. Throughput denotes end-to-end training throughput (forward and backward passes). Parameter counts report predictor parameters only.

E. Interpretability Analysis

We analyze the behavior of the pre-trained Adaptive SBLU, focusing on its estimations of the frequency and decay. Figure 4 illustrates the input spectrogram of a sample from

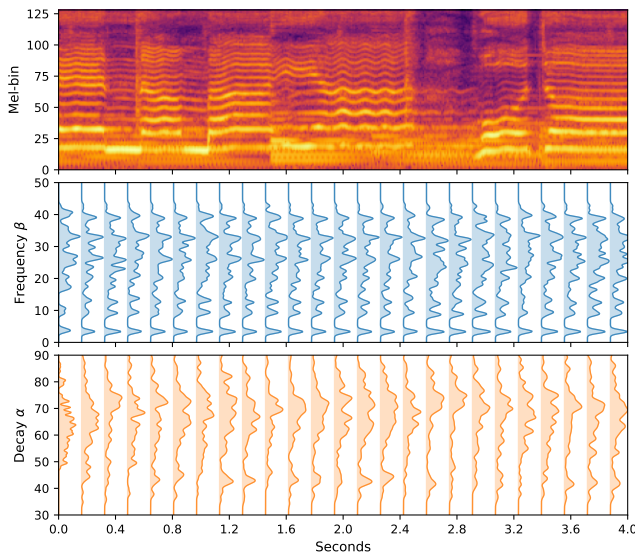


Fig. 4: **Example of Patch-wise Adaptive Estimation of SBLU Kernel Parameters.** Top: input spectrogram prior to patchification, which is subsequently patchified and fed into the Lambda Encoder. Middle/Bottom: per-time-patch distributions of the estimated SBLU kernel parameters (decay and frequency) produced by the pre-trained Lambda Encoder, showing adaptive variation in response to the input.

the AudioSet [16] dataset, along with the distributions of frequency and decay estimated by the pre-trained Lambda Encoder for that input. In our experimental setup, note that the Adaptive SBLU estimates 16 pairs of frequency and decay for each patch. Regarding frequency, the distribution is spread widely across all frequency bands, indicating that the model successfully extracts information from various aliasing-prone bands. The decay distribution is skewed toward larger values, indicating a preference for higher temporal resolution over frequency resolution. However, lower values also occur at certain time points, indicating that the model occasionally prioritizes frequency resolution depending on the situation. These findings demonstrate that Adaptive SBLU conducts frequency feature analysis in a flexible manner, dynamically adjusting the balance between temporal and frequency resolution in response to the input characteristics.

V. CONCLUSION

This work addresses aliasing caused by aggressive spectrogram patchification in transformer-based audio models. We propose Aliasing-aware Patch Embedding (AaPE), implemented via a Structured Bilateral Laplace Unit (SBLU) inspired by structured state-space models. SBLU employs a two-sided exponential window to execute dynamic subband frequency analysis, integrating aliasing-related features with standard patch tokens. This approach aims to mitigate aliasing without compromising task-relevant high-frequency content. AaPE serves as a drop-in replacement for ViT-style patch tokens and is pre-trained on AudioSet with teacher-student masked audio modeling, a multi-mask strategy, and a contrastive regularization.

AaPE consistently improves fine-tuning performance across diverse audio benchmarks and tasks, outperforming or equal-

ing state-of-the-art self-supervised baselines while maintaining competitiveness under linear probing. These trends suggest that frequency-sensitive feature extraction is effective for periodic, quasi-stationary audio. However, tasks dominated by fine-grained pitch dynamics or significantly short contexts may require complementary mechanisms. AaPE targets an architectural bottleneck at the input stage, making it orthogonal to the other (architectural- and augmentation-based) SSL methods. This characteristic naturally lends itself to combination with these methods. The limitations of this approach include the reliance on log-mel inputs, emphasis on amplitude-modulation cues, and reduced gains on extremely short utterances or pitch-dominated tasks. Future work will combine AaPE with stronger pre-training strategies and extending SBLU to better capture pitch-varying/chirp patterns and very short contexts.

REFERENCES

- [1] J. Devlin, M.-W. Chang, K. Lee, and K. Toutanova, “Bert: Pre-training of deep bidirectional transformers for language understanding,” in *Conference of the North American Chapter of the Association for Computational Linguistics (NAACL)*, 2019.
- [2] M. Oquab, T. Darcet, T. Moutakanni, H. V. Vo, M. Szafraniec, V. Khalidov, P. Fernandez, D. Haziza, F. Massa, A. El-Nouby, R. Howes, P.-Y. Huang, H. Xu, V. Sharma, S.-W. Li, W. Galuba, M. Rabbat, M. Assran, N. Ballas, G. Synnaeve, I. Misra, H. Jegou, J. Mairal, P. Labatut, A. Joulin, and P. Bojanowski, “Dinov2: Learning robust visual features without supervision,” 2023.
- [3] P.-Y. Huang, H. Xu, J. Li, A. Baevski, M. Auli, W. Galuba, F. Metze, and C. Feichtenhofer, “Masked autoencoders that listen,” in *Advances in Neural Information Processing Systems (NeurIPS)*, 2022.
- [4] A. Baade, P. Peng, and D. Harwath, “MAE-AST: Masked Autoencoding Audio Spectrogram Transformer,” in *Annual Conference of the International Speech Communication Association (INTERSPEECH)*, 2022, pp. 2438–2442.
- [5] Y. Gong, C.-I. Lai, Y.-A. Chung, and J. Glass, “SSAST: Self-Supervised Audio Spectrogram Transformer,” in *AAAI Conference on Artificial Intelligence (AAAI)*, vol. 36, no. 10, 2022, pp. 10 699–10 709.
- [6] X. Li, N. Shao, and X. Li, “Self-supervised audio teacher-student transformer for both clip-level and frame-level tasks,” *IEEE/ACM Transactions on Audio, Speech, and Language Processing*, vol. 32, pp. 1336–1351, 2023.
- [7] D. Niizumi, D. Takeuchi, Y. Ohishi, N. Harada, and K. Kashino, “Masked modeling duo: Towards a universal audio pre-training framework,” *IEEE/ACM Transactions on Audio, Speech, and Language Processing*, vol. 32, pp. 2391–2406, 2024.
- [8] Y. Gong, Y.-A. Chung, and J. Glass, “AST: Audio Spectrogram Transformer,” in *Annual Conference of the International Speech Communication Association (INTERSPEECH)*, 2021, pp. 571–575.
- [9] A. Dosovitskiy, L. Beyer, A. Kolesnikov, D. Weissenborn, X. Zhai, T. Unterthiner, M. Dehghani, M. Minderer, G. Heigold, S. Gelly, J. Uszkoreit, and N. Houlsby, “An image is worth 16x16 words: Transformers for image recognition at scale,” in *International Conference on Learning Representations (ICLR)*, 2021.
- [10] K. He, X. Chen, S. Xie, Y. Li, P. Dollár, and R. Girshick, “Masked Autoencoders Are Scalable Vision Learners,” in *IEEE/CVF Conference on Computer Vision and Pattern Recognition (CVPR)*, June 2022, pp. 16 000–16 009.
- [11] A. Bruguier, A. Misra, A. Narayanan, and R. Prabhavalkar, “Anti-aliasing regularization in stacking layers,” in *Annual Conference of the International Speech Communication Association (INTERSPEECH)*, 2020, pp. 314–318.
- [12] E. Fonseca, A. Ferraro, and X. Serra, “Improving sound event classification by increasing shift invariance in convolutional neural networks,” *arXiv:2107.00623*, 2021.
- [13] R. Zhang, “Making convolutional networks shift-invariant again,” in *International Conference on Machine Learning (ICML)*. PMLR, 2019, pp. 7324–7334.
- [14] A. Gu, K. Goel, and C. Ré, “Efficiently modeling long sequences with structured state spaces,” in *International Conference on Learning Representations (ICLR)*, 2022.

- [15] A. Gu, K. Goel, A. Gupta, and C. Ré, “On the parameterization and initialization of diagonal state space models,” *Advances in Neural Information Processing Systems (NeurIPS)*, vol. 35, pp. 35 971–35 983, 2022.
- [16] J. F. Gemmeke, D. P. Ellis, D. Freedman, A. Jansen, W. Lawrence, R. C. Moore, M. Plakal, and M. Ritter, “Audio set: An ontology and human-labeled dataset for audio events,” in *IEEE International Conference on Acoustics, Speech, and Signal Processing (ICASSP)*. IEEE, 2017, pp. 776–780.
- [17] K. J. Piczak, “Esc: Dataset for environmental sound classification,” in *ACM International Conference on Multimedia (ACM MM)*, ser. MM ’15. New York, NY, USA: Association for Computing Machinery, 2015, pp. 1015–1018.
- [18] J. Salamon, C. Jacoby, and J. P. Bello, “A dataset and taxonomy for urban sound research,” in *ACM International Conference on Multimedia (ACM MM)*, 2014, pp. 1041–1044.
- [19] J. Engel, C. Resnick, A. Roberts, S. Dieleman, M. Norouzi, D. Eck, and K. Simonyan, “Neural audio synthesis of musical notes with wavenet autoencoders,” in *International Conference on Machine Learning (ICML)*. PMLR, 2017, pp. 1068–1077.
- [20] P. Warden, “Speech commands: A dataset for limited-vocabulary speech recognition,” *arXiv:1804.03209*, 2018.
- [21] H. Cao, D. G. Cooper, M. K. Keutmann, R. C. Gur, A. Nenkova, and R. Verma, “Crema-d: Crowd-sourced emotional multimodal actors dataset,” *IEEE Transactions on Affective Computing*, vol. 5, no. 4, pp. 377–390, 2014.
- [22] D. Chong, H. Wang, P. Zhou, and Q. Zeng, “Masked spectrogram prediction for self-supervised audio pre-training,” in *IEEE International Conference on Acoustics, Speech, and Signal Processing (ICASSP)*. IEEE, 2023, pp. 1–5.
- [23] S. Chen, Y. Wu, C. Wang, S. Liu, D. Tompkins, Z. Chen, W. Che, X. Yu, and F. Wei, “BEATS: audio pre-training with acoustic tokenizers,” in *International Conference on Machine Learning (ICML)*, 2023.
- [24] S. A. A. Ahmed, M. Awais, W. Wang, M. D. Plumbley, and J. Kittler, “Asit: Local-global audio spectrogram vision transformer for event classification,” *IEEE/ACM Transactions on Audio, Speech, and Language Processing*, vol. 32, pp. 3684–3693, 2024.
- [25] W. Chen, Y. Liang, Z. Ma, Z. Zheng, and X. Chen, “Eat: Self-supervised pre-training with efficient audio transformer,” in *International Joint Conference on Artificial Intelligence (IJCAI)*, K. Larson, Ed. IJCAI, 8 2024, pp. 3807–3815, main Track.
- [26] J. Wang, T. Wang, M. Ge, L. Wang, and J. Dang, “ASDA: Audio Spectrogram Differential Attention Mechanism for Self-Supervised Representation Learning,” in *Annual Conference of the International Speech Communication Association (INTERSPEECH)*, 2025, pp. 5803–5807.
- [27] T. Alex, S. Atito, A. Mustafa, M. Awais, and P. J. B. Jackson, “SSLAM: Enhancing self-supervised models with audio mixtures for polyphonic soundscapes,” in *International Conference on Learning Representations (ICLR)*, 2025.
- [28] A. Baevski, Y. Zhou, A. Mohamed, and M. Auli, “wav2vec 2.0: A framework for self-supervised learning of speech representations,” in *Advances in Neural Information Processing Systems (NeurIPS)*, vol. 33, 2020, pp. 12 449–12 460.
- [29] W.-N. Hsu, B. Bolte, Y.-H. H. Tsai, K. Lakhotia, R. Salakhutdinov, and A. rahman Mohamed, “Hubert: Self-supervised speech representation learning by masked prediction of hidden units,” *IEEE/ACM Transactions on Audio, Speech, and Language Processing*, vol. 29, pp. 3451–3460, 2021.
- [30] A. Gu and T. Dao, “Mamba: Linear-time sequence modeling with selective state spaces,” *arXiv:2312.00752*, 2023.
- [31] N. Zeghidour, O. Teboul, F. de Chaumont Quitry, and M. Tagliasacchi, “Leaf: A learnable frontend for audio classification,” in *International Conference on Learning Representations (ICLR)*, 2021.
- [32] J. Schlüter and G. Gutenbrunner, “Efficientleaf: A faster learnable audio frontend of questionable use,” in *European Signal Processing Conference (EUSIPCO)*, 2022, pp. 205–208.
- [33] V. Lostanlen, D. Haider, H. Han, M. Lagrange, P. Balazs, and M. Ehler, “Fitting auditory filterbanks with multiresolution neural networks,” in *IEEE Workshop on Applications of Signal Processing to Audio and Acoustics (WASPAA)*, 2023, pp. 1–5.
- [34] M. Anderson, T. H. Kinnunen, and N. Harte, “Learnable frontends that do not learn: Quantifying sensitivity to filterbank initialisation,” in *IEEE International Conference on Acoustics, Speech, and Signal Processing (ICASSP)*, 2023, pp. 1–5.
- [35] B. Hayes, C. Saitis, and G. Fazekas, “Sinusoidal frequency estimation by gradient descent,” in *IEEE International Conference on Acoustics, Speech, and Signal Processing (ICASSP)*, 2023, pp. 1–5.
- [36] L. Fu, L. Lian, R. Wang, B. Shi, X. Wang, A. Yala, T. Darrell, A. A. Efros, and K. Goldberg, “Rethinking patch dependence for masked autoencoders,” *arXiv:2401.14391*, 2024.
- [37] T. Chen, S. Kornblith, M. Norouzi, and G. Hinton, “A simple framework for contrastive learning of visual representations,” in *International Conference on Machine Learning (ICML)*, ser. Proceedings of Machine Learning Research, H. D. III and A. Singh, Eds., vol. 119. PMLR, 13–18 Jul 2020, pp. 1597–1607.
- [38] I. Loshchilov and F. Hutter, “Decoupled weight decay regularization,” in *International Conference on Learning Representations (ICLR)*, 2019.
- [39] —, “Sgdr: Stochastic gradient descent with warm restarts,” in *International Conference on Learning Representations (ICLR)*, 2017.
- [40] H. Bao, L. Dong, S. Piao, and F. Wei, “Beit: Bert pre-training of image transformers,” *arXiv:2106.08254*, 2021.
- [41] H. Zhang, M. Cisse, Y. N. Dauphin, and D. Lopez-Paz, “mixup: Beyond empirical risk minimization,” in *International Conference on Learning Representations (ICLR)*, 2018.
- [42] G. Huang, Y. Sun, Z. Liu, D. Sedra, and K. Q. Weinberger, “Deep networks with stochastic depth,” in *European Conference on Computer Vision (ECCV)*, 2016.
- [43] D. S. Park, W. Chan, Y. Zhang, C.-C. Chiu, B. Zoph, E. D. Cubuk, and Q. V. Le, “SpecAugment: A simple data augmentation method for automatic speech recognition,” in *Annual Conference of the International Speech Communication Association (INTERSPEECH)*, 2019.
- [44] A. Baevski, W.-N. Hsu, Q. Xu, A. Babu, J. Gu, and M. Auli, “data2vec: A General Framework for Self-supervised Learning in Speech, Vision and Language,” in *International Conference on Machine Learning (ICML)*, 2022, pp. 1298–1312.
- [45] A. Quelenec, P. Chouteau, G. Peeters, and S. Essid, “Masked latent prediction and classification for self-supervised audio representation learning,” in *IEEE International Conference on Acoustics, Speech, and Signal Processing (ICASSP)*, 2025, pp. 1–5.

APPENDIX A

We derive Eq. (2) under the notation and conventions specified in the main text (see Sec. III-B). Applying the integrating factor $e^{-\mathbf{A}t}$ to the continuous-time linear state equation $\frac{d}{dt}\mathbf{h}(t) = \mathbf{A}\mathbf{h}(t) + \mathbf{B}\mathbf{u}(t)$ and integrating from 0 to s yields

$$\mathbf{h}(s) = e^{\mathbf{A}s}\mathbf{h}(0) + \int_0^s e^{\mathbf{A}(s-t)}\mathbf{B}\mathbf{u}(t) dt, \quad (\text{A.1})$$

with the initial condition $\mathbf{h}(0) = 0$. As a modeling choice to obtain a symmetric representation (two-sided exponential window) centered at $s/2$, we write

$$\mathbf{h}(s) = \int_0^s e^{-\mathbf{A}|t-\frac{s}{2}|}\mathbf{B}\mathbf{u}(t) dt, \quad (\text{A.2})$$

which, upon splitting at $s/2$, becomes

$$\mathbf{h}(s) = e^{-\frac{\mathbf{A}s}{2}} \int_0^{\frac{s}{2}} e^{\mathbf{A}t}\mathbf{B}\mathbf{u}(t) dt + e^{\frac{\mathbf{A}s}{2}} \int_{\frac{s}{2}}^s e^{-\mathbf{A}t}\mathbf{B}\mathbf{u}(t) dt. \quad (\text{A.3})$$

Let $s = (n+1)\Delta$ with $n = K-1$, and apply zero-order-hold (ZOH) discretization. We obtain

$$\begin{aligned} \mathbf{h}[K] &= e^{-\frac{1}{2}\Delta\mathbf{A}(n+1)} \sum_{k=0}^c \left(\int_{k\Delta}^{(k+1)\Delta} e^{\mathbf{A}t} dt \right) \mathbf{B}\mathbf{u}[k] \\ &\quad + e^{\frac{1}{2}\Delta\mathbf{A}(n+1)} \sum_{k=c+1}^{K-1} \left(\int_{k\Delta}^{(k+1)\Delta} e^{-\mathbf{A}t} dt \right) \mathbf{B}\mathbf{u}[k] \\ &= e^{-\frac{1}{2}\Delta\mathbf{A}} \mathbf{A}^{-1} (e^{\Delta\mathbf{A}} - \mathbf{I}) \sum_{k=0}^c e^{\Delta\mathbf{A}(k-c)} \mathbf{B}\mathbf{u}[k] \\ &\quad + e^{\frac{1}{2}\Delta\mathbf{A}} \mathbf{A}^{-1} (\mathbf{I} - e^{-\Delta\mathbf{A}}) \sum_{k=c+1}^{K-1} e^{\Delta\mathbf{A}(c-k)} \mathbf{B}\mathbf{u}[k], \end{aligned} \quad (\text{A.4})$$

using $\int_{k\Delta}^{(k+1)\Delta} e^{\pm\Lambda t} dt = \pm\mathbf{A}^{-1}e^{\pm\Delta\Lambda k}(e^{\pm\Delta\Lambda} - \mathbf{I})$. With the eigen-decomposition and identities $\mathbf{A} = \mathbf{P}\mathbf{\Lambda}\mathbf{P}^{-1}$, $e^{\mathbf{A}} = \mathbf{P}e^{\mathbf{\Lambda}}\mathbf{P}^{-1}$, $\sinh\left(\frac{1}{2}\Delta\mathbf{\Lambda}\right) = \frac{1}{2}\left(e^{\frac{1}{2}\Delta\mathbf{\Lambda}} - e^{-\frac{1}{2}\Delta\mathbf{\Lambda}}\right)$, we obtain

$$\begin{aligned} \mathbf{h}[K] &= \mathbf{P}e^{-\frac{1}{2}\Delta\mathbf{\Lambda}}\mathbf{\Lambda}^{-1}(e^{\Delta\mathbf{\Lambda}} - \mathbf{I})\sum_{k=0}^c e^{\Delta\mathbf{\Lambda}(k-c)}\mathbf{P}^{-1}\mathbf{B}\mathbf{u}[k] \\ &\quad + \mathbf{P}e^{\frac{1}{2}\Delta\mathbf{\Lambda}}\mathbf{\Lambda}^{-1}(\mathbf{I} - e^{-\Delta\mathbf{\Lambda}})\sum_{k=c+1}^{K-1} e^{\Delta\mathbf{\Lambda}(c-k)}\mathbf{P}^{-1}\mathbf{B}\mathbf{u}[k] \\ &= 2\mathbf{P}\mathbf{\Lambda}^{-1}\sinh\left(\frac{\Delta\mathbf{\Lambda}}{2}\right)\sum_{k=0}^{K-1} e^{-\Delta\mathbf{\Lambda}|k-c|}\overline{\mathbf{B}}\mathbf{u}[k], \quad (\text{A.5}) \end{aligned}$$

where $\overline{\mathbf{B}} = \mathbf{P}^{-1}\mathbf{B}$. Finally, regarding $\mathbf{h}[K]$ as the representative value at the center index of the n -th sliding window, and applying the observation equation $\mathbf{y}[n] = \mathbf{C}\mathbf{h}[n]$, we obtain

$$\mathbf{y}[n] = 2\overline{\mathbf{C}}\mathbf{\Lambda}^{-1}\sinh\left(\frac{\Delta\mathbf{\Lambda}}{2}\right)\sum_{k=0}^{K-1} e^{-\Delta\mathbf{\Lambda}|k-c|}\overline{\mathbf{B}}\mathbf{u}[n+k-c], \quad (\text{A.6})$$

with $\overline{\mathbf{C}} = \mathbf{C}\mathbf{P}$.

APPENDIX B

We derive the normalization coefficient $\gamma_i \geq 0$ in Eq. (4). Let $\lambda_i = \alpha_i + j\beta_i$ with $\alpha_i, \beta_i \in \mathbb{R}$ and $j^2 = -1$. For the diagonal elements of the complex diagonal matrix $\mathbf{\Lambda}^{-1}\sinh\left(\frac{\Delta\mathbf{\Lambda}}{2}\right)$, namely $\lambda_i^{-1}\sinh\left(\frac{\Delta\lambda_i}{2}\right)$, employing the identity for a complex argument of $\sinh(\cdot)$ (and Euler's formula) yields

$$\begin{aligned} \sinh\left(\frac{\Delta\lambda_i}{2}\right) &= \sinh\left(\frac{\Delta\alpha_i}{2}\right)\cos\left(\frac{\Delta\beta_i}{2}\right) \\ &\quad + j\cosh\left(\frac{\Delta\alpha_i}{2}\right)\sin\left(\frac{\Delta\beta_i}{2}\right). \quad (\text{B.1}) \end{aligned}$$

Using $\cosh^2(\cdot) - \sinh^2(\cdot) = 1$, we obtain

$$\gamma_i = \left|\lambda_i^{-1}\sinh\left(\frac{\Delta\lambda_i}{2}\right)\right| = \sqrt{\frac{\cosh^2\left(\frac{\Delta\alpha_i}{2}\right) - \cos^2\left(\frac{\Delta\beta_i}{2}\right)}{\alpha_i^2 + \beta_i^2}}. \quad (\text{B.2})$$

Equivalently, noting that for $a, b \in \mathbb{R}$, $|\sinh(a + jb)|^2 = \sinh^2 a \cos^2 b + \cosh^2 a \sin^2 b = \cosh^2 a - \cos^2 b$, the non-negativity $\gamma_i \geq 0$ follows immediately, and the denominator is positive since $|\lambda_i| > 0$ by the imposed bounding constraints.

APPENDIX C

We illustrate, in a scalar example, the coupling that enables convolution reuse in Adaptive SBLU (see Sec. III-C): the real-part gradient with respect to the decay α and the imaginary-part gradient with respect to the frequency β share an identical convolution; likewise, the real-part gradient with respect to β and the imaginary-part gradient with respect to α share an identical convolution. For an input $x_n \in \mathbb{R}$ at time index n with parameters α_n (decay) and β_n (frequency), define the

magnitude output $|y_n| = \sqrt{\text{Re}(y_n)^2 + \text{Im}(y_n)^2}$. The real and imaginary parts are

$$\text{Re}(y_n) = \sum_{k=0}^{K-1} x_{n+k-c} \cdot e^{-\Delta_k \alpha_n} \cos(\Delta_k \beta_n) \quad (\text{C.1})$$

$$\text{Im}(y_n) = \sum_{k=0}^{K-1} x_{n+k-c} \cdot e^{-\Delta_k \alpha_n} \sin(\Delta_k \beta_n) \quad (\text{C.2})$$

with $\Delta_k = \Delta|k-c|$. Setting $R_n = \frac{\text{Re}(y_n)}{|y_n|}$ and $I_n = \frac{\text{Im}(y_n)}{|y_n|}$, the real-part gradients of $|y_n|$ are

$$\text{Re}\left(\frac{\partial|y_n|}{\partial\alpha_n}\right) = -R_n \sum_{k=0}^{K-1} \Delta_k x_{n+k-c} e^{-\Delta_k \alpha_n} \cos(\Delta_k \beta_n) \quad (\text{C.3})$$

$$\text{Re}\left(\frac{\partial|y_n|}{\partial\beta_n}\right) = -R_n \sum_{k=0}^{K-1} \Delta_k x_{n+k-c} e^{-\Delta_k \alpha_n} \sin(\Delta_k \beta_n) \quad (\text{C.4})$$

and the imaginary-part gradients are

$$\text{Im}\left(\frac{\partial|y_n|}{\partial\alpha_n}\right) = -I_n \sum_{k=0}^{K-1} \Delta_k x_{n+k-c} e^{-\Delta_k \alpha_n} \sin(\Delta_k \beta_n) \quad (\text{C.5})$$

$$\text{Im}\left(\frac{\partial|y_n|}{\partial\beta_n}\right) = I_n \sum_{k=0}^{K-1} \Delta_k x_{n+k-c} e^{-\Delta_k \alpha_n} \cos(\Delta_k \beta_n) \quad (\text{C.6})$$

from which the following coupling relations follow, halving the convolutional workload:

$$\text{Re}\left(\frac{\partial|y_n|}{\partial\alpha_n}\right) = -\frac{R_n}{I_n} \text{Im}\left(\frac{\partial|y_n|}{\partial\beta_n}\right), \quad (\text{C.7})$$

$$\text{Re}\left(\frac{\partial|y_n|}{\partial\beta_n}\right) = \frac{R_n}{I_n} \text{Im}\left(\frac{\partial|y_n|}{\partial\alpha_n}\right). \quad (\text{C.8})$$

Finally, the gradients are

$$\begin{aligned} \frac{\partial|y_n|}{\partial\alpha_n} &= \text{Re}\left(\frac{\partial|y_n|}{\partial\alpha_n}\right) + \text{Im}\left(\frac{\partial|y_n|}{\partial\alpha_n}\right) \\ &= \text{Re}\left(\frac{\partial|y_n|}{\partial\alpha_n}\right) + \frac{I_n}{R_n} \text{Re}\left(\frac{\partial|y_n|}{\partial\beta_n}\right), \quad (\text{C.9}) \end{aligned}$$

$$\begin{aligned} \frac{\partial|y_n|}{\partial\beta_n} &= \text{Re}\left(\frac{\partial|y_n|}{\partial\beta_n}\right) + \text{Im}\left(\frac{\partial|y_n|}{\partial\beta_n}\right) \\ &= \text{Re}\left(\frac{\partial|y_n|}{\partial\beta_n}\right) - \frac{I_n}{R_n} \text{Re}\left(\frac{\partial|y_n|}{\partial\alpha_n}\right). \quad (\text{C.10}) \end{aligned}$$

In implementation, it suffices to compute once per n the two base convolutions

$$S_c(n) = \sum_{k=0}^{K-1} \Delta_k x_{n+k-c} e^{-\Delta_k \alpha_n} \cos(\Delta_k \beta_n), \quad (\text{C.11})$$

$$S_s(n) = \sum_{k=0}^{K-1} \Delta_k x_{n+k-c} e^{-\Delta_k \alpha_n} \sin(\Delta_k \beta_n), \quad (\text{C.12})$$

and reuse them across the four partial gradients via the coupling relations above, reducing compute and memory traffic.